Journal of Zhejiang University-SCIENCE A in press
www.jzus.zju.edu.cn; www.springer.com/journal/11582
E-mail: jzus_a@zju.edu.cn

Research Article
https://doi.org/10.1631/jzus.A2600099

Dynamics of a two-disk dynamo loaded with a dual neuron circuit and its application

Fuqiang WU[1,2]✉, Ying XU[3], Huimin QI[1], Jun MA[4]

[1]*School of Mathematics and Statistics, Ningxia University, Yinchuan 750021, China*
[2]*Ningxia Basic Science Research Center of Mathematics, Yinchuan 750021, China*
[3]*School of Mathematics and Statistics, Shandong Normal University, Ji'nan 250014, China*
[4]*Department of Physics, Lanzhou University of Technology, Lanzhou 730050, China*

Abstract: Constructing a neuromorphic electromechanical system based on a flexible memristor is of great significance for the development of biomimetic electrical-mechanical transverters. A bioinspired electromechanical system can perform real-time energy-efficient processing of multimodal signals, including electrical activities and mechanical motions. Here, we propose a bioinspired electromechanical system composed of a two-disc dynamo driven by a dual integrate-and-fire neuron. A memristive system exists in the bioinspired electromechanical system, as observed in the current-voltage relationship. The neuromorphic electromechanical model can exhibit a multiscroll hidden attractor by adjusting a controllable parameter. Complex chaotic behaviors have been demonstrated by numerical simulations, including two-parameter bifurcation, Lyapunov exponents, and phase diagrams. Finally, the applicability of a chaotic encryption scheme is successfully implemented on a neuromorphic electromechanical system.

Key words: Nonlinear dynamics; electromechanical system; memristor; encryption

1 Introduction

Bioinspired memristive systems have emerged as promising candidates for developing neuromorphic circuits with analog electrical activities (Lei et al., 2025; Kamsma et al., 2023; Yang et al., 2024; Ma, 2025). For example, neuromorphic memristive circuits based on VO_2 material can not only exhibit neuronal excitability and bursting patterns associated with saddle nodes on invariant cycles and Hopf bifurcations but also achieve phase synchronization and locomotion rhythms (Shao et al., 2025a, 2025b; Bonagiri et al., 2024; Dutta et al., 2019). Memristive Josephson junction circuits can generate neuronal dynamical behaviors, including excitability, spiking, bursting, in-phase/antiphase bursting synchronizations, and spatiotemporal patterns (Wu et al., 2023a, 2024; Wu and Yao, 2023b; Wu and Feng, 2025). Based on the electromagnetic effect induced by the exchange of ionic currents, memristive coupled neuronal models can exhibit a wide range of firing modes and collective behaviors (An and Qiao, 2021; Yang et al., 2023; Wu et al., 2022; Xu et al., 2018, 2023). Double-membrane neuronal models composed of two capacitors and memristors have been proposed to describe biophysical functions and behaviors (Li et al., 2024; Feng et al., 2025; Bao et al., 2023; Yang et al., 2024). The complex oscillating modes obtained from dynamical systems hold relatively greater value in technological applications because of their high randomness and unpredictability. In recent years, chaotic dynamical systems have been introduced into image encryption to enhance information security issues (An et al., 2023, 2024; Lai and Liu, 2025; Yang et al., 2022).

To interact with electronic devices effectively, advanced neuromorphic circuits should be equipped with an electromechanically transformed module that

✉ Fuqiang WU, alexwutian@nxu.edu.cn
Fuqiang WU, https://orcid.org/0000-0002-3850-7400
Huimin QI, https://orcid.org/0009-0000-9433-8130
Jun MA, https://orcid.org/0000-0002-6127-000X

Received Mar. 1, 2026; Revision accepted Apr. 22, 2026;
Crosschecked

can convert between multimodal motions and abundant electrical activities (Kitio Kwuimy and Woafo, 2007, 2008; Drapaca, 2015; Mbeunga et al., 2021; Mboussi et al., 2014; Kouami et al., 2020). An electromechanical system integrates electrical and mechanical components to convert electrical energy into mechanical motion, or vice versa, enabling it to perform precise, automated, or controlled tasks. Disk dynamo is a classic model in the electromechanical system, illustrating the interplay between electromagnetic induction and mechanical motion. The homopolar dynamo consisting of rotating disks and associated coils can perform oscillations of constant amplitude (Bullard, 1955). When a disk rotates, it cuts magnetic field lines, generating a motional electromotive force (EMF). This EMF drives a current in the coil, which in turn produces a magnetic field. The interaction between the mechanical rotation and the electromagnetic effects is at the heart of the disk dynamo. An improved electromechanical model consisting of two coupled disk dynamos was proposed to generate chaotic behaviors (Rikitake, 1958). Two-disk dynamo models with an emerging chaotic switching sequence were employed to reveal the sequence of reversals of the Earth's magnetic field (Cox, 1968; Cook and Roberts, 1970; Ito, 1980; Ershov et al., 1989; Donato et al., 2009). The dynamo is crucial for understanding self-sustaining magnetic field generation, offering insights into how mechanical energy can be converted into electrical energy and how electromagnetic systems can exhibit complex dynamical behaviors.

The nervous system can generate neuronal electrical signals to convert mechanical signals into control signals for muscles. An electromotor driven by the neural circuit is employed to mimic arm contraction (Guo et al., 2025a). Electromechanical systems with a pair of jointed pendulums have been proposed to represent the movements of artificial muscles (Guo and Ma, 2025b; Guo et al., 2024; Ma and Guo, 2024). Neuromorphic circuits are introduced into electromechanical systems to emulate the effective and rapid response of muscle contraction and relaxation. In this paper, we propose a novel electromechanical system comprising a two-disk dynamo and a dual neuromorphic circuit. The electromechanical system can produce complex oscillated rhythms. Based on the chaotic sequence of the electromechanical system, an improved image encryption scheme is proposed to explore the real-world applicability of the neuromorphic electromechanical model.

2 Model

To study the coupled two-disk dynamo loaded with dual integrate-and-fire (IF) neurons, as shown in Fig. 1a, we make the following assumptions and conduct modeling from both circuit and dynamics perspectives. It is assumed that the two disks and their connected coils have the same physical parameters, including radius r, moment of inertia J, inductance L, resistance R, and the number of turns per unit length of coil n. Both discs are subjected to the same constant external torque N, and the coils are regarded as infinitely long straight solenoids.

When the left disc 1 rotates, it generates a magnetic field $B_1=\mu_0 nI_1$ at the position of the right disc. Similarly, when the right disc 2 rotates, it generates a magnetic field $B_2=\mu_0 nI_2$ at the position of the left disc, where μ_0 is the vacuum permeability, and I_1 and I_2 are the coil currents. When the left disc rotates at angular velocity ω_1, for a line element dl at radial distance l from the axis, the left motional electromotive force is

$$\mathrm{d}\varepsilon_1 = (\vec{v}_1 \times \vec{B}_2)\bullet \mathrm{d}\vec{l} = l\omega_1 B_2 \mathrm{d}l. \tag{1}$$

Integrating this, the total motional electromotive force for the left disc is obtained as

$$\varepsilon_1 = \int_0^r l\omega_1 B_2 \mathrm{d}l = kI_2\omega_1, \tag{2}$$

where $k=0.5\mu_0 nr^2$ is a constant determined by the geometric and electromagnetic properties of the disc and the coil, with r denoting the radius of the disc and n the number of turns in the coil. Similarly, when the right disc rotates at angular velocity ω_2, the total motional electromotive force for the right disc is $\varepsilon_2=kI_1\omega_2$. This derivation establishes the bidirectional electromagnetic coupling between the two rotating discs: the rotation of one disc induces an electromotive force in the other disc via the generated magnetic field, which forms the core

electromechanical interaction of the system. For the subsequent circuit modeling, we adopt the following physically justified simplifications: the mutual inductance between the two coils is neglected (as the induced motional electromotive force dominates the coupling dynamics in this disc dynamo configuration), while the self-inductance of each coil is fully considered to accurately describe the current evolution in the circuit. Based on the above electromotive force expressions and simplifying assumptions, the circuit equations for the two-disc dynamo system, which is further coupled to a dual IF neuron model as illustrated in Fig. 1b, are derived as follows:

$$\begin{cases} C_1 \dfrac{\mathrm{d}V_1}{\mathrm{d}t} = I_{ext} - \dfrac{V_1}{R_1} + I_1, \\ L_1 \dfrac{\mathrm{d}I_1}{\mathrm{d}t} = V_1 - I_1 r_1 + \varepsilon_1, \\ C_2 \dfrac{\mathrm{d}V_2}{\mathrm{d}t} = -\dfrac{V_2}{R_2} + I_2, \\ L_2 \dfrac{\mathrm{d}I_2}{\mathrm{d}t} = V_2 - I_2 r_2 + \varepsilon_2, \end{cases} \tag{3}$$

which describes the relationship between the induced motional electromotive force, self-inductive motional electromotive force, and the membrane potential across the IF neuron.

Fig. 1 provides a comprehensive illustration of the proposed neuromorphic electromechanical system, including both its physical structure and equivalent circuit representation. Panel (a) depicts the bidirectional coupling mechanism between the two disks and the dual IF neurons: the rotation of each disk generates a magnetic field that induces electromotive forces in the other disk, while the neurons modulate the electrical currents across the system. This structure explicitly demonstrates how mechanical rotation (angular velocity ω_1, ω_2) and neural activity (membrane potential V_1, V_2) are integrated in a unified framework. Panel (b) presents the corresponding equivalent circuit, which consists of standard circuit elements (resistors, capacitors, inductors) together with velocity-dependent inductive memristors. This circuit model quantifies the electromagnetic coupling and provides a mathematical basis for deriving the system's dynamic equations.

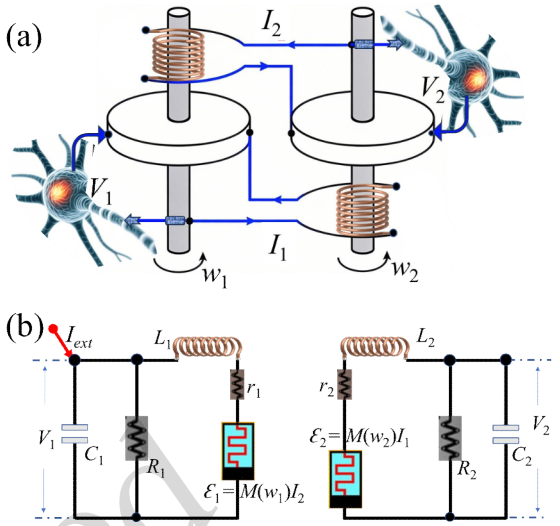

Fig. 1 Schematic diagram of the proposed two-disk neuromorphic electromechanical system (a) Physical structure showing the bidirectional electromagnetic coupling between the two rotating disks and their coupling to the dual IF neurons, where I_1 and I_2 represent the coil currents, ω_1 and ω_2 denote the angular velocities of the disks, and V_1 and V_2 are the membrane potentials of the corresponding neurons. (b) Equivalent circuit model of the system, comprising inductors L_1 and L_2, resistors R_1 and R_2, capacitors C_1 and C_2, and inductive memristors $\varepsilon_1=M(\omega_1)I_2$ and $\varepsilon_2=M(\omega_2)I_1$ that are modulated by the angular velocities.

The line element of the left disc is subjected to a resistance force as

$$\mathrm{d}\vec{f}_1 = I_1 \mathrm{d}\vec{l} \times \vec{B}_2, \tag{4}$$

from which the electromagnetic damping torque $N_1=kI_1I_2$ is derived. Similarly, the electromagnetic damping torque of the right disc is $N_2=kI_1I_2$. There is no friction at the rotation axes of the two discs, and they are subjected to an external torque N. Combined with the rotational law, the dynamic equations are obtained as

$$\begin{cases} J \dfrac{\mathrm{d}\omega_1}{\mathrm{d}t} = N - kI_1I_2, \\ J \dfrac{\mathrm{d}\omega_2}{\mathrm{d}t} = N - kI_1I_2, \end{cases} \tag{5}$$

where J is the moment of inertia. ω_1 and ω_2 are the

angular velocities. Subtracting the two dynamic equations gives $\mathrm{d}(\omega_1-\omega_2)/\mathrm{d}t=0$, that is, $\omega_1-\omega_2=c_0$ (where c is a constant). Let $\omega_1=\omega+0.5c_0$ and $\omega_2=\omega-0.5c_0$; then, the dynamic equation is simplified to

$$J\frac{\mathrm{d}\omega}{\mathrm{d}t}=N-kI_1I_2. \tag{6}$$

By combining the circuit equations in Eq. (3) with the simplified dynamic equation in Eq. (6), based on Kirchhoff's theorem, the model of a two-disk dynamo loaded with a dual integrate-and-fire neuron is expressed by

$$J\frac{\mathrm{d}\omega}{\mathrm{d}t}=N-kI_1I_2. \tag{7}$$

where the physical parameters (C_1, L_1, C_2, L_2, J, I_{ext}, R_1, r_1, R_2, r_2, N, k) are selected with suitable values, and this model can be adjusted to present complex bursting, spiking, and even chaotic patterns. By observing the model in Eq. (7), there exist two memristors that can be expressed as

$$J\frac{\mathrm{d}\omega}{\mathrm{d}t}=N-kI_1I_2. \tag{8}$$

These physical variables are replaced with dimensionless variables under scale transformation as

$$J\frac{\mathrm{d}\omega}{\mathrm{d}t}=N-kI_1I_2. \tag{9}$$

The mathematical model of a two-disk dynamo loaded with dual integrate-and-fire neurons is described by

$$J\frac{\mathrm{d}\omega}{\mathrm{d}t}=N-kI_1I_2. \tag{10}$$

The appearance of the memristive term introduces more adjustable parameters into the biophysical model, and the normalized parameters (d_1, d_2) are relative to the property of coupled discs.

3 Numerical results and discussion

3.1 Dynamics of a memristive system

There are two memristors in the neuromorphic electromechanical system. The important property is the appearance of a pinched hysteretic loop in the current-voltage characteristics of the simplified memristive model subjected to a periodical input.

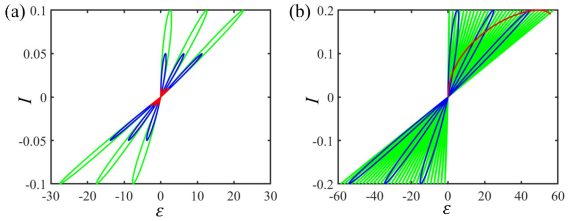

Fig. 2 Current-voltage (I-ε) hysteresis characteristics of the simplified memristor model under periodic sinusoidal input signals $I=A\sin(2\pi f\tau)$, where A denotes the input amplitude and f represents the signal frequency. (a) Hysteresis loops obtained at a fixed frequency f=0.01 with varying amplitudes: green, blue, and red curves correspond to A=0.1, A=0.05, and A=0.01, respectively. (b) Hysteresis loops obtained at a fixed amplitude A=0.2 with varying frequencies: green, blue, and red curves correspond to f=0.1, f=0.01, and f=0.001, respectively.

Fig. 2 illustrates the current-voltage hysteresis characteristics of a simplified memristor model under periodic input signals. The currents through the two memristors are assumed to be equal, i.e., $I_1=I_2=I$, and the voltage is denoted as ε. To characterize the memristive behavior, periodic sinusoidal input signals $I=A\sin(2\pi f\tau)$ are applied, where A and f are the input amplitude and frequency, respectively. Fig. 2a presents the hysteresis curves under a fixed low frequency f=0.01 with varying amplitudes. It is clearly observed that the area enclosed by the hysteresis loop monotonically increases with the input amplitude A, a typical signature of memristive devices. Fig. 2b further explores the frequency dependence of the hysteresis behavior at a fixed amplitude A=0.2. The results demonstrate that the area of the hysteresis loop gradually decreases as the frequency f increases, and the I-ε curve converges to the characteristic of a nonlinear resistor when the frequency approaches an infinitesimal value. These findings fully validate the memristive nature of the adopted model, laying a solid physical foundation for the subsequent dynamical analysis of the coupled electromechanical-neuronal system and its application in chaotic encryption.

3.2 Dynamics of a neuromorphic electromechanical system

Based on the theoretical analysis in the electronic supplementary materials, the system exhibits chaotic dynamics and dissipative properties when the parameters are selected to m_0=1 and I_{ext}=0.05.

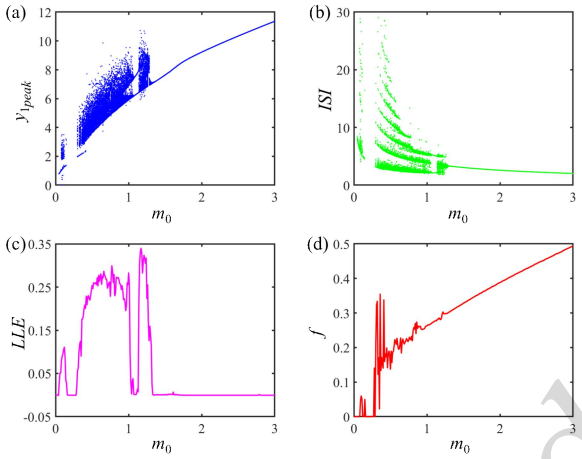

Fig. 3 (a) Dynamic characteristics of the electromechanical system versus parameter m_0 with i_{ext}=0.05. (a) One-parameter bifurcation diagram. (b) ISI bifurcation diagram. (c) LLE spectra. (d) Frequency diagram. Other parameters are selected at g_1=100, a_1=0.05, g_2=100, b_1=100, c=300, d_1=200, g_3=100, a_2=0.05, g_4=100, b_2=100, d_2=200, g_5=1, and e=0.5.

Fig. 3 presents a comprehensive analysis of the dynamical behaviors of the electromechanical system with respect to parameter m_0, including a one-parameter bifurcation diagram, an interspike interval (ISI) bifurcation diagram, the largest Lyapunov exponent (LLE) spectrum, and a frequency diagram. Specifically, Fig. 3a shows the one-parameter bifurcation diagram, which directly reveals the transition routes among the resting state, chaotic oscillation, and period-1 motion as m_0 increases. Fig. 3b displays the ISI bifurcation diagram, which further verifies the evolution of firing intervals corresponding to different dynamical states. Correspondingly, as shown in Fig. 3c, the electromechanical system exhibits chaotic behaviors when the LLE is greater than zero. When the LLE is less than zero, it indicates that the electromechanical system is in a state of rest. Similarly, in the resting state, the system exhibits a zero frequency. In the chaotic regime, the frequency fluctuates markedly, reflecting pronounced instability. In the periodic region, the frequency remains stable and is significantly elevated. Thus, the dynamical transitions of the electromechanical system are dependent upon the parameter m_0.

Fig. 4 presents the time series diagram of state variables (x_1, x_2, y_1, y_2) (as shown in Figs. 4a, 4b, 4d, and 4e) and the phase diagram of the state variable (x_2-x_1, y_2-y_1) (as shown in Figs. 4c and 4f) of the electromechanical system. Specifically, observing the amplification window of the time series diagram, we find that the system exhibits continuous nonperiodic fluctuations over time. The corresponding phase diagram shows complex and irregular limit cycles. These characteristics verify that the electromechanical system is in a chaotic state when m_0=1.

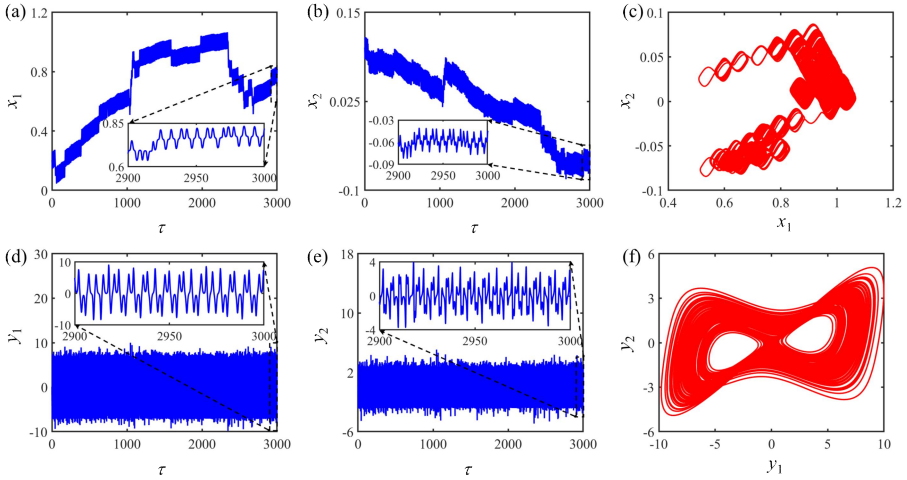

Fig. 4 Dynamical behaviors of the proposed neuromorphic electromechanical system. (a, b, d, e) Time series of the state variables x_1, x_2, y_1, y_2, respectively, with insets showing magnified views of the steady-state fluctuations. (c, f)

Corresponding phase-plane portraits in the (x_1, x_2) and (y_1, y_2) planes. The parameters are selected as m_0=1, g_1=100, a_1=0.05, g_2=100, b_1=100, c=300, d_1=200, g_3=100, a_2=0.05, g_4=100, b_2=100, d_2=200, g_5=1, and e=0.5, while fixed at i_{ext}=0.05.

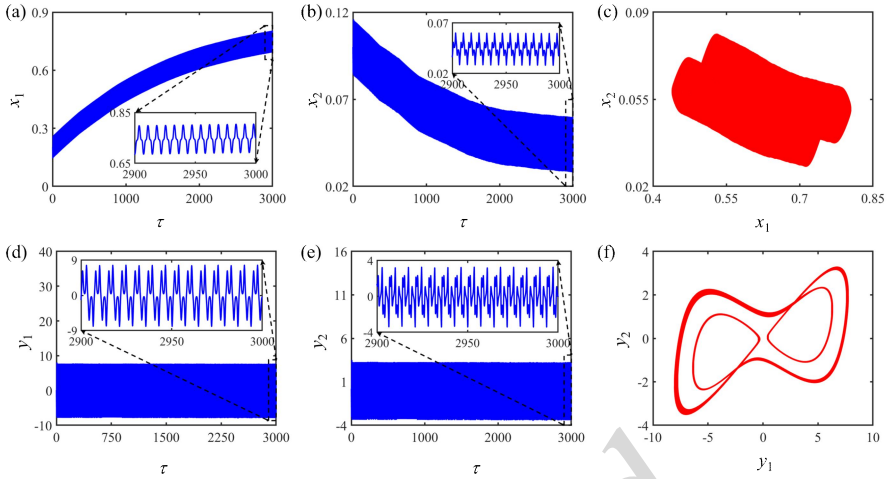

Fig. 5 Dynamical behaviors of the proposed neuromorphic electromechanical system. (a, b, d, e) Time series of the state variables x_1, x_2, y_1, y_2, respectively, with insets showing magnified views of the steady-state fluctuations. (c, f) Corresponding phase-plane portraits in the (x_1, x_2) and (y_1, y_2) planes. The parameters are selected as m_0=1.1, g_1=100, a_1=0.05, g_2=100, b_1=100, c=300, d_1=200, g_3=100, a_2=0.05, g_4=100, b_2=100, d_2=200, g_5=1, and e=0.5, while fixed at i_{ext}=0.05.

Fig. 5 presents the time series diagram of the state variable (x_1, x_2, y_1, y_2) (as shown in Figs. 5a, 5b, 5d, and 5e) and the phase diagram of the state variable (x_2-x_1, y_2-y_1) (as shown in Figs. 5c and 5f) of the electromechanical system when the parameter m_0=1.1. Combined with the time series and phase trajectory, it can be seen that the system exhibits a period-2 oscillation when m_0=1.1. This conclusion is entirely consistent with the various analysis results in Fig. 3, which further verifies the authenticity and consistency of the system dynamics behavior.

Fig. 6 illustrates the time series diagram of state variables (x_1, x_2, y_1, y_2) (as shown in Figs. 6a, 6b, 6d and 6e) and the phase diagram of the state variables (x_2-x_1, y_2-y_1) (as shown in Figs. 6c and 6f)) of the electromechanical system at m_0=2.6. The time trajectory exhibits a strictly repetitive waveform with a single period, whereas the phase diagram displays a single, closed limit cycle orbit. This indicates that the system exhibits a stable period-1 oscillation state at m_0=2.6. The above dynamic characteristics are highly consistent with the multidimensional index analysis results shown in Fig. 3, which thoroughly verifies the reliability and consistency of the observed system response.

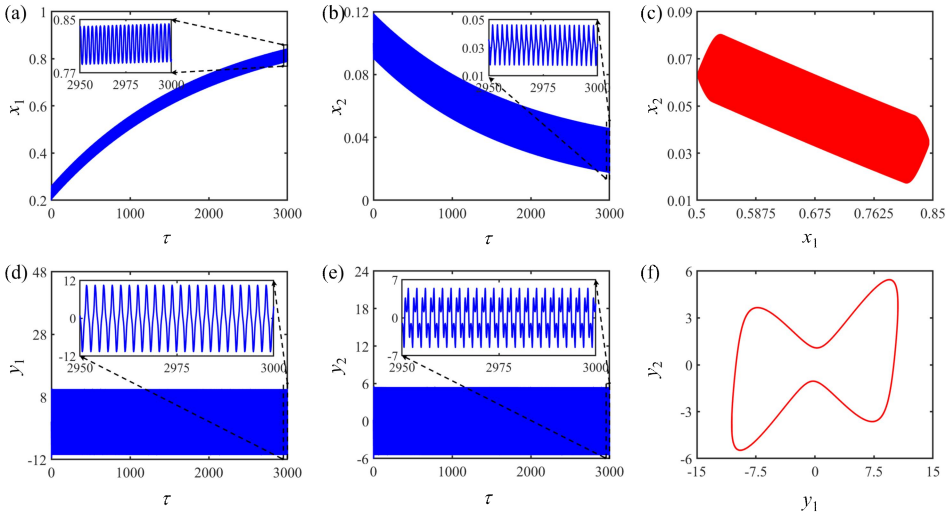

Fig. 6 Dynamical behaviors of the proposed neuromorphic electromechanical system. (a, b, d, e) Time series of the state variables x_1, x_2, y_1, y_2, respectively, with insets showing magnified views of the steady-state fluctuations. (c, f) Corresponding phase-plane portraits in the (x_1, x_2) and (y_1, y_2) planes. The parameters are selected as m_0=2.6, g_1=100, a_1=0.05, g_2=100, b_1=100, c=300, d_1=200, g_3=100, a_2=0.05, g_4=100, b_2=100, d_2=200, g_5=1, and e=0.5, while fixed at i_{ext}=0.05.

Fig. 7 illustrates a comprehensive analysis of the dynamical behaviors of the electromechanical system with respect to parameter i_{ext}, including the one-parameter bifurcation diagram, ISI bifurcation diagram, LLE spectra, and frequency diagram. In particular, according to LLE, which remains positive in the interval from 0 to 3, it can be seen that the system is always in a chaotic state during the increasing process of i_{ext}. At the same time, the oscillation frequency exhibits significant random fluctuations within the range, further confirming that the system possesses the characteristics of a chaotic attractor. The above results clearly demonstrate that the external stimulus current has a significant nonlinear effect on the electromechanical system. To further confirm the reliability of the above conclusions, the time series and phase trajectory are numerically fitted, as shown in Fig. 8.

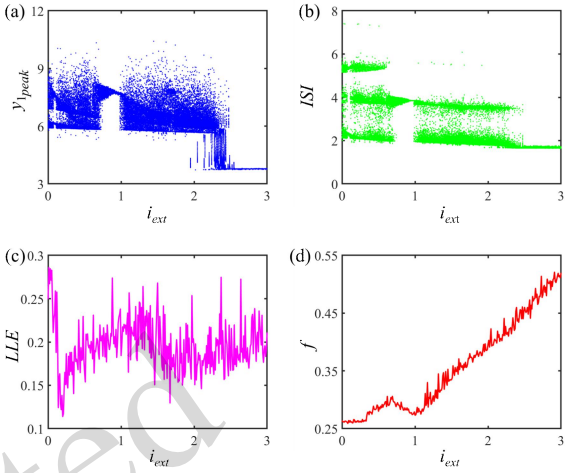

Fig. 7 Dynamical transition characteristics of the electromechanical system versus parameter i_{ext} with m_0=1. (a) One-parameter bifurcation diagram. (b) ISI bifurcation diagram. (c) LLE spectra. (d) Frequency diagram. Other parameters are selected at g_1=100, a_1=0.05, g_2=100, b_1=100, c=300, d_1=200, g_3=100, a_2=0.05, g_4=100, b_2=100, d_2=200, g_5=1, and e=0.5.

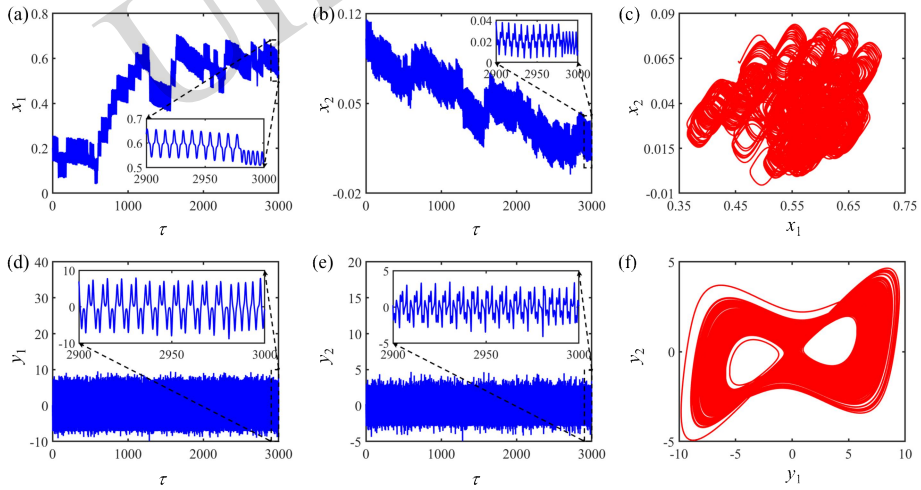

Fig. 8 Dynamical behaviors of the proposed neuromorphic electromechanical system. (a, b, d, e) Time series of the state variables x_1, x_2, y_1, y_2, respectively, with insets showing magnified views of the steady-state fluctuations. (c, f) Corresponding phase-plane portraits in the (x_1, x_2) and (y_1, y_2) planes. The parameters are selected as i_{ext}=0, g_1=100, a_1=0.05, g_2=100, b_1=100, c=300, d_1=200, g_3=100, a_2=0.05, g_4=100, b_2=100, d_2=200, g_5=1, and e=0.5, while fixed at m_0=1.

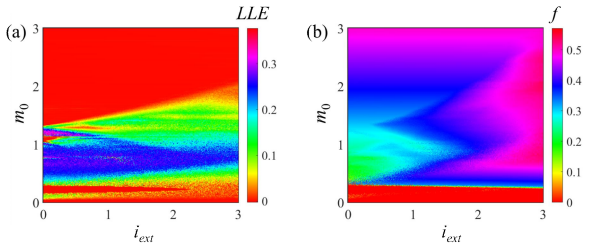

Fig. 9 Two-parameter diagrams of the electromechanical system described by Eq. (10) with respect to the external current i_{ext} and parameter m_0; (a) LLE distribution; (b) average frequency f distribution. Parameters are set as m_0=1, g_1=100, a_1=0.05, g_2=100, b_1=100, c=300, d_1=200, g_3=100, a_2=0.05, g_4=100, b_2=100, d_2=200, g_5=1, e=0.5, and i_{ext}=0.05.

Fig. 8 presents the time series diagram of state variables (x_1, x_2, y_1, y_2) (as shown in Figs. 8a, 8b, 8d and 8e) and the phase diagram of the state variables (x_2-x_1, y_2-y_1) (as shown in Figs. 8c and 8f)) of the electromechanical system when i_{ext}=0. It can be seen from the time series diagram that the state variables x_1, x_2, y_1, and y_2 oscillate nonperiodically with time, and the waveform shows obvious nonrepetitive and irregular characteristics, and the amplitude still maintains violent fluctuations in the long-term evolution process. The phase trajectory diagram exhibits a diffuse and complex structure, with no closed limit cycle formed, further confirming that the system is in a chaotic state. These results are entirely consistent with the characteristics of various indicators shown in Fig. 7, which verifies the correctness and consistency of the chaotic behavior of the system under the condition of i_{ext}=0.

Fig. 9 further explores the two-parameter bifurcation characteristics of the electromechanical system in Eq. (10), systematically investigating the combined effects of the external current i_{ext} and the parameter m_0 on the system's nonlinear dynamics. Fig. 9a presents the distribution of the LLE, which serves as a quantitative indicator for judging chaotic motion. The color gradient clearly shows that positive LLE values dominate a large portion of the parameter plane, confirming the widespread existence of chaotic behavior in the proposed system. Fig. 9b displays the corresponding average oscillation frequency f, revealing how the frequency distribution evolves with varying i_{ext} and m_0. The consistency between the two-parameter results in Fig. 9 and the single-parameter bifurcation analyses (Figs. 3c and 3d) and 7(c, d)) further validates the reliability and accuracy of the numerical results. Overall, Fig. 9 not only demonstrates the rich dynamical complexity of the neuromorphic electromechanical system but also identifies key parameter ranges where chaotic signals are sufficiently strong. This provides essential guidance for selecting appropriate parameters in the design of chaotic encryption systems, as discussed in the following sections.

3.3 Image encryption based on the neuromorphic electromechanical system

This section discusses an application of the proposed neuromorphic electromechanical system to image encryption. The encryption and decryption process of the image is shown in Fig. 10.

Fig. 10 provides a comprehensive overview of the complete workflow for the proposed chaotic image encryption and decryption scheme, which integrates the electromechanical chaotic system with DNA computing. The blue upper section details the encryption process: the input color image is first decomposed into independent red (R), green (G), and blue (B) channels. Each channel undergoes image segmentation processing, followed by DNA encoding to convert pixel values into DNA sequences. These sequences are then subjected to DNA operations, which are strictly controlled by the pseudorandom chaotic sequences generated from the previously validated electromechanical chaotic system. After DNA decoding and a final row-column permutation step, the encrypted ciphertext image is produced, which appears as noise and is resistant to unauthorized access. The green lower section outlines the symmetric decryption process, which reverses all encryption steps in the correct order, using the same chaotic sequences to recover the original plaintext image. This flowchart explicitly demonstrates the bidirectional, secure nature of the algorithm, with the electromechanical chaotic system serving as the core cryptographic primitive that ensures the high sensitivity, large key space, and strong security of the entire encryption scheme, laying a clear structural foundation for the detailed performance analysis presented in subsequent sections. The detailed mechanism of the DNA encryption and decryption process will be analyzed below.

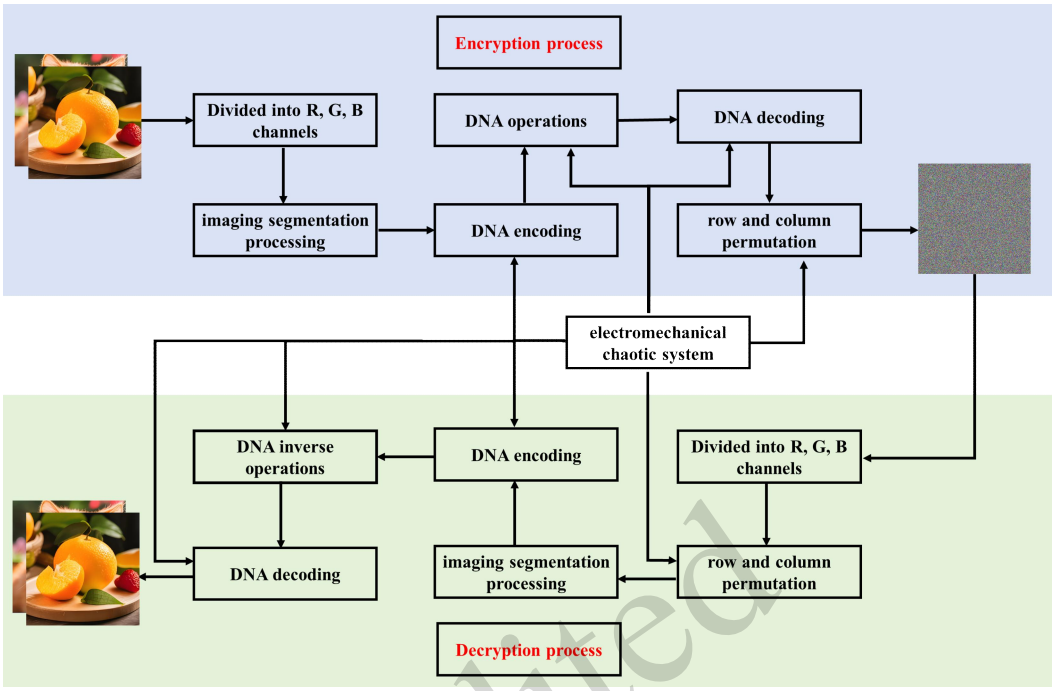

Fig. 10 Flowchart of the proposed chaotic image encryption and decryption scheme based on the electromechanical chaotic system and DNA operations. The blue-shaded region denotes the encryption process. The green-shaded region represents the symmetric decryption process.

In the DNA encryption algorithm, the input $M\times N$ color image is first preprocessed and divided into three independent gray channels: red (R), green (G), and blue (B). The pixel value range of each channel is 0 to 255. Then, a random key sequence K with a length of $M\times N$ and a range of 0 to 255 is generated. Its randomness and confidentiality are the keys to encryption security. Then, the pixel values $P_{i,j}$ of each channel are encrypted, and the encrypted pixel values $C_{i,j}$ are calculated by the formula $C_{i,j}=(P_{i,j}+K_{i,j})$ mod 256 to ensure that the encrypted pixel values remain in the range of 0 to 255. Then, a mapping rule is defined to map each encrypted pixel value to a specific DNA sequence, so that the encrypted pixel values of the R, G, and B channels are converted into the corresponding DNA sequences DR, DG, and DB, respectively. Finally, these DNA sequences are stored or synthesized by biotechnology for subsequent decryption. The whole process makes full use of the biological characteristics of DNA and the enormous information storage capacity, which provides an innovative and efficient method for the secure encryption of image information.

In the DNA decryption algorithm, the image decryption process includes the following steps. First, three independent DNA sequences were extracted from stored or synthesized DNA samples, corresponding to red (R), green (G), and blue (B) color channels. Then, according to the mapping rules consistent with the encryption, these DNA sequences (DR, DG, and DB) are converted into the corresponding encrypted pixel values CR, CG, and CB. Then, the encrypted pixel values $C_{i,j}$ of each color channel are decrypted. The decrypted pixel values $P_{i,j}$ are calculated by using the formula $P_{i,j}=(C_{i,j}-K_{i,j})$ mod 256, where $K_{i,j}$ are the values of the corresponding positions in the key sequence used for encryption. The consistency of the key sequence is the key to successful decryption. Finally, image reconstruction is performed to create a blank image with a size of $M\times N$, and the decrypted R, G, and B channel pixel values are filled into the corresponding channels to restore the original color image. This process verifies the efficiency and reliability of DNA encryption technology in the field of information security.

To systematically evaluate the performance of the proposed DNA algorithm, we employ three metrics in this section: the histogram, interr-adjacent pixel correlation, and information entropy.

In the field of image encryption, histogram

analysis serves as a crucial statistical metric for evaluating algorithm performance, as it intuitively reveals the distribution of pixel values in an image. A histogram uses pixel values as the horizontal axis and the frequency or number of corresponding pixel values as the vertical axis. By counting the frequency of distribution of each pixel value, a discrete bar chart is formed. For a plaintext image, its histogram typically exhibits an irregular and uneven pattern, which may provide vulnerabilities for attackers. A core objective of encryption is to eliminate such statistical properties of the plaintext through confusion and diffusion mechanisms, thereby resisting statistical analysis attacks. A well-performing encryption algorithm should produce a ciphertext image with a highly uniform histogram, approximating the distribution of random noise. This paper employs histogram analysis to evaluate the performance of the proposed DNA-based encryption algorithm. By converting pixel values into nucleotide sequences and performing nonlinear operations, the algorithm effectively disrupts the correlation among pixels in the plaintext image, achieving excellent diffusion. Therefore, a more uniform histogram distribution of the encrypted image demonstrates superior confusion and diffusion properties, significantly enhancing the resistance against statistical attacks.

Correlation analysis between adjacent pixels is another key statistical measure for evaluating the performance of image encryption algorithms. It measures the linear dependence between adjacent pixel values in the horizontal, vertical, or diagonal directions of the image. Plain images typically exhibit strong spatial correlation in these directions, meaning that adjacent pixel values are highly similar, thereby forming a smooth visual contour. Because of this, this correlation is often used by attackers for statistical analysis attacks to crack encryption algorithms. In DNA image encryption, the use of this index aims to quantify the effectiveness of the encryption algorithm in destroying this spatial correlation through its obfuscation and diffusion mechanism. The DNA encryption algorithm converts pixel values into base sequences through complex algebraic operations and nonlinear transformations, and performs highly randomized processing. This process not only completely disrupts the statistical structure of the original plaintext but also effectively removes the correlation between adjacent pixels, rendering the encrypted image statistically indistinguishable from a random distribution.

In the field of image encryption, information entropy is used to measure the degree of disorder in the distribution of pixel values within an image. The higher the information entropy value is, the more uniform the pixel value distribution, the closer it is to a random distribution, and the greater the uncertainty of the information contained in the image. Therefore, high information entropy means that the encryption system has a stronger ability to resist statistical attacks. This paper introduces this index to evaluate the effectiveness of the DNA encryption algorithm in randomizing plaintext images. The algorithm randomizes the pixel value of the original image through algebraic operations and nonlinear transformations based on DNA coding rules, thereby improving the information entropy of the encrypted image. We can evaluate the performance of the DNA algorithm by comparing the information entropy of the plaintext image and the encrypted image. Suppose the information entropy of the encrypted image is significantly higher than that of the plain image. In that case, the DNA algorithm effectively increases the randomness of the image and improves the security of the encryption. The information entropy of the output ciphertext of an encryption algorithm with excellent performance should be very close to the theoretical maximum value of 8. The closer the calculation result is to 8, the more equal the probability of each pixel value in the ciphertext, the stronger the randomness, and the better the confusion effect of the algorithm on the plaintext.

To intuitively verify the effectiveness of the DNA encryption algorithm proposed in this paper, this section focuses on the test images of a cat and fruits, and comprehensively analyzes the above indicators in the form of visual maps (histograms and adjacent pixel correlations) and data tables (information entropy).

Fig. 11 presents the histogram analysis results for cat images. Specifically, Fig. 11a displays the plaintext cat image, and Fig. 11b shows the cat image after encryption, which becomes indistinguishable and exhibits characteristics of random noise. This is the intended effect of the encryption algorithm, which

is designed to protect the image content from unauthorized access. Fig. 11c is the decrypted image, which has been restored to a state similar to the original image, confirming the effectiveness of the encryption and decryption processes. Figs. 11d and 11f corresponds to the histograms of the red (R), green (G), and blue (B) color channels of the plaintext cat image, respectively. The pixel value distribution of each channel exhibits a distinct concentration trend, reflecting the characteristics of the color distribution in the original image. Figs. 11g–11i illustrates the pixel value distribution of the red, green, and blue color channels in the encrypted image. Compared to the plaintext image, the pixel value distribution of the encrypted image is more uniform and closer to a random distribution. This phenomenon indicates that the encryption algorithm effectively disrupts the statistical characteristics of the original image, making it difficult to recognize or analyze, thereby significantly increasing the randomness of the image and enhancing the security of the encryption. Furthermore, this improved randomness also demonstrates the good performance of the encryption algorithm in terms of confusion and diffusion, further ensuring the protection of the image content.

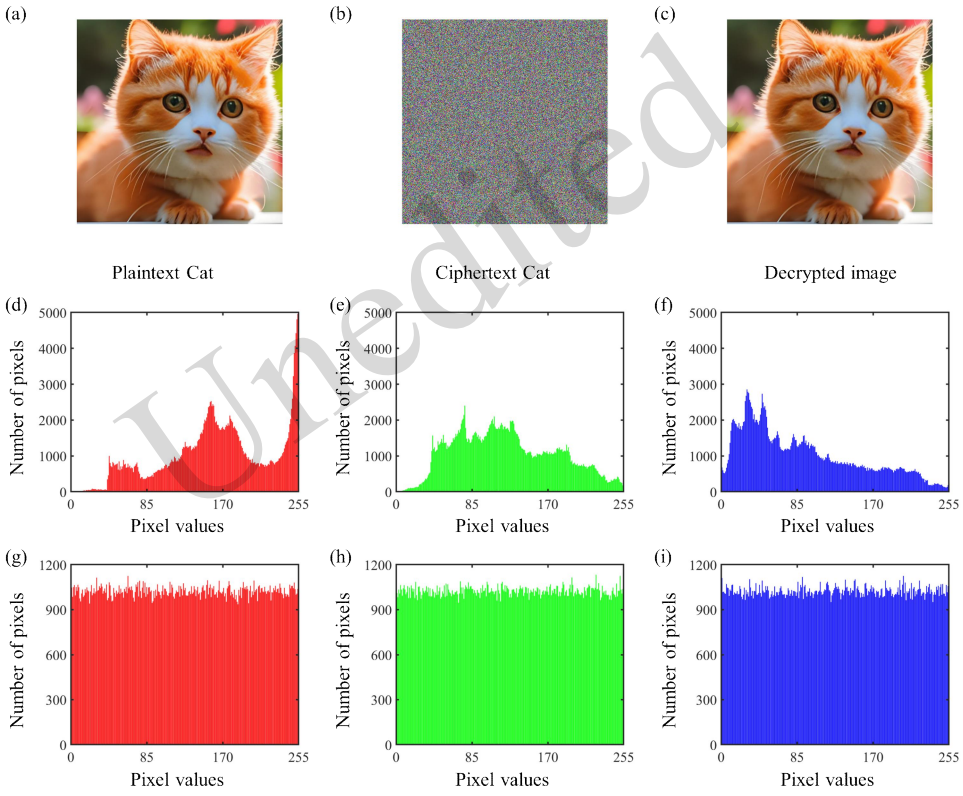

Fig. 11 Histogram analysis results of the proposed chaotic image encryption scheme using the cat image as the plaintext. (a) Plaintext cat; (b) Ciphertext cat; (c) Decrypted image; (d-f) The histogram of the R channel, G channel and B channel of the plaintext cat image; (g-i) The histogram of the R channel, G channel and B channel of the ciphertext cat image.

Fig. 12 shows the correlation analysis results between adjacent pixels in the cat image. Specifically, Figs. 12a–12c shows the pixel correlation distribution of the three-color channels of red (R), green (G), and blue (B) in the horizontal, vertical, and diagonal directions of the cat image. Figs. 12d–12f shows the pixel correlation distribution of the encrypted image in the same direction. In Figs. 12a–12c, the pixel correlation of the plaintext image exhibits obvious linear characteristics, indicating a high correlation between adjacent pixels in the plaintext image. This correlation is uniformly visible in the horizontal, vertical, and diagonal directions, reflecting the inherent statistical laws in each color channel in the plain image. In contrast, the encrypted images (Figs. 12d–12f) show significantly different correlation distributions. In the encrypted image, the correlation between adjacent pixels is reduced dramatically, and

the scatter distribution tends to be random and evenly distributed throughout the range. This change is consistent in all directions, indicating that the DNA encryption algorithm effectively destroys the spatial correlation between the pixels of the plaintext image and significantly enhances the randomness and security of the image.

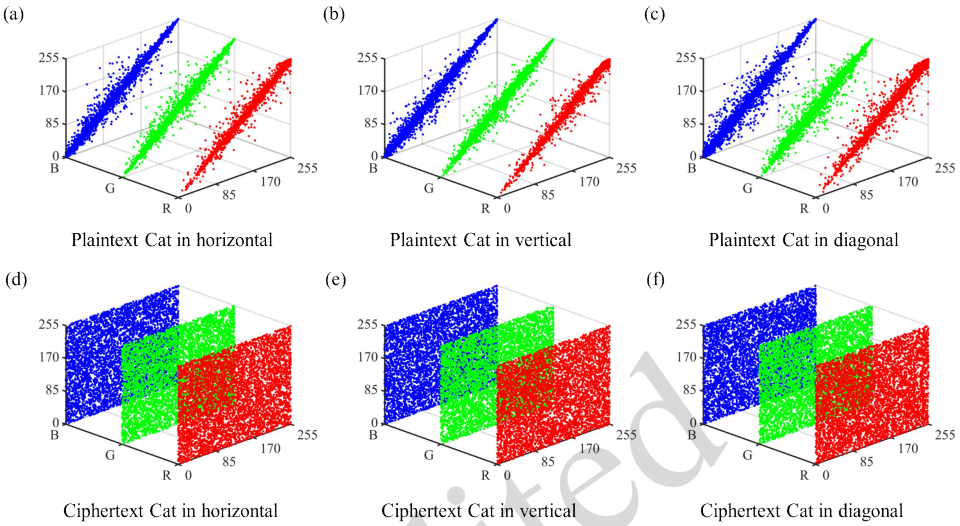

Fig. 12 Correlation analysis of adjacent pixels in the R, G, and B channels of the plaintext and ciphertext cat images, evaluated in the horizontal, vertical, and diagonal directions. (a-c) Correlation distributions of the R, G, B channels for the plaintext cat image in the horizontal, vertical, and diagonal directions, respectively; (d-f) Correlation distributions of the R, G, B channels for the ciphertext cat image under the same directional conditions.

Fig. 13 provides the results of the histogram analysis of fruit images. Figs. 13a–13c shows the plaintext fruit image, the encrypted ciphertext image, and the decrypted image, respectively. The content of the encrypted image becomes unrecognizable, and the decrypted image is highly similar to the original plaintext image, which verifies the effectiveness of the encryption and decryption process. Figs. 13d–13f and (g-i) depict the pixel value distribution of the plain and ciphertext fruit images on the three color channels of red (R), green (G), and blue (B), respectively. By comparing these two sets of histograms, we can observe that the pixel value distribution of each color channel in the plain image shows a specific concentration trend, which reflects the characteristics of the color distribution in the original image. In contrast, the pixel value distribution of the ciphertext image is more uniform and closer to a random distribution. This phenomenon demonstrates that the encryption algorithm effectively disrupts the statistical characteristics of the original image, making it difficult to identify or analyze the image content, thereby significantly enhancing the randomness of the image and improving the security of the encryption.

Fig. 14 shows the correlation analysis results between adjacent pixels in the fruit image. Figs. 14a–14c is the pixel correlation distribution of the three-color channels of red (R), green (G), and blue (B) in the horizontal, vertical, and diagonal directions of the plain fruit image. Figs. 14d–14f corresponds to the pixel correlation distribution of the ciphertext fruit image in the same direction. In the plain image, the pixel correlation exhibits a clear linear trend, indicating a strong correlation between adjacent pixels. In the encrypted image, the correlation distribution becomes random and scattered, indicating that the encryption algorithm effectively destroys the correlation between pixels and enhances the image's randomness, thereby improving the encryption's security. These results further verify the good performance of the encryption algorithm in terms of confusion and diffusion.

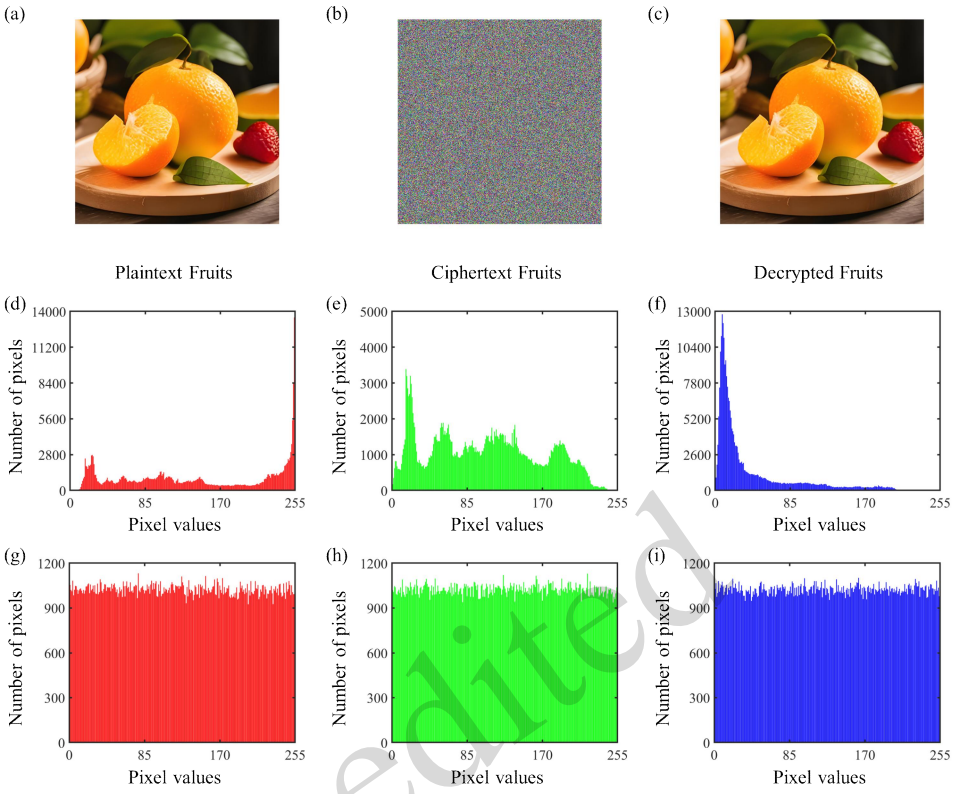

Fig. 13 Histogram analysis results of the proposed chaotic image encryption scheme using the fruit image as the plaintext. (a) Plaintext fruits; (b) Ciphertext fruits; (c) Decrypted image; (d-f) The histogram of the R channel, G channel, and B channel of the plaintext fruit image; (g-i) The histogram of the R channel, G channel, and B channel of the cyphertext fruit image.

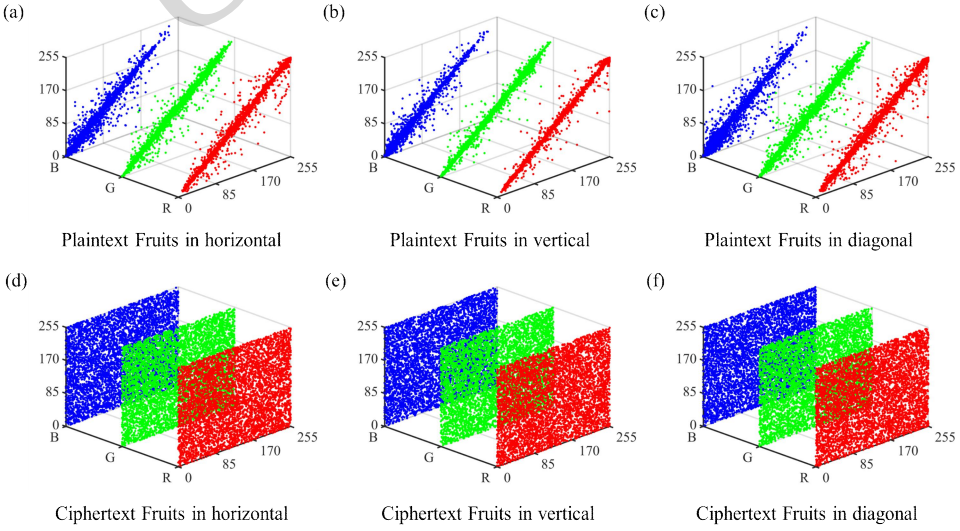

Fig. 14 Correlation analysis of adjacent pixels in the R, G, and B channels of the plaintext and ciphertext fruit images, evaluated in the horizontal, vertical, and diagonal directions. (a-c) Correlation distributions of the R, G, B channels for the plaintext fruit image in the horizontal, vertical, and diagonal directions, respectively; (d-f) Correlation distributions of the R, G, B channels for the ciphertext fruit image under the same directional conditions.

To intuitively evaluate the performance of the DNA encryption algorithm at the data level, we display the correlation coefficients and information entropies of different images in tabular form, as

shown in Tables 1 and 2.

Table 1 presents the correlation coefficients of the red (R), green (G), and blue (B) color channels in the horizontal (H), vertical (V), and diagonal (D) directions for the images (cat and fruit). In the plain image, the correlation coefficient of each image is generally close to 1, indicating a strong correlation between adjacent pixels, a typical feature of natural images. After encryption, the correlation coefficient is significantly reduced, approaching zero or exhibiting a slight negative correlation, indicating that the encryption algorithm effectively destroys the correlation between pixels and substantially improves the image's randomness. The comparison results show that the DNA encryption algorithm performs well in reducing the correlation of image pixels, thereby enhancing the security performance of image encryption. Therefore, the algorithm has a significant impact on disturbing the statistical characteristics of the image and enhancing the security of encryption, which has considerable reference value for evaluating the effectiveness of the encryption algorithm.

Table 2 presents the information entropy values of cat and fruit images in both plaintext and ciphertext states for the red, green, and blue color channels. The information entropy value of the plaintext image varies between different images and color channels, indicating an uneven distribution of the original image information. In contrast, the information entropy of the ciphertext image is close to the theoretical maximum value of 8, indicating that the encrypted image information is more evenly distributed. The encryption process significantly improves the image information entropy and enhances the randomness of the ciphertext image, thereby improving security, because high information entropy means stronger unpredictability. The improvement of information entropy also reflects the effectiveness of the encryption algorithm in increasing the uncertainty of image data, which helps to resist attacks by analyzing data patterns. Therefore, the data in Table 2 demonstrate the effectiveness of the encryption algorithm in enhancing image information entropy and improving encryption security, which is a key indicator for evaluating the algorithm's performance.

Table 1 Calculated correlation coefficients for different images

Images	Direction	Plaintext image			Ciphertext image		
		R	G	B	R	G	B
Cat	H	0.9921	0.9890	0.9899	−0.0062	0.0085	0.0133
	V	0.9889	0.9850	0.9859	0.0000	−0.0025	0.0059
	D	0.9825	0.9758	0.9770	0.0031	0.0063	−0.0094
Fruit	H	0.9966	0.9930	0.9806	−0.0077	−0.0078	0.0063
	V	0.9945	0.9899	0.9754	−0.0041	−0.0064	0.0042
	D	0.9918	0.9850	0.9642	−0.0018	0.0042	0.0020

Table 2 Information entropy calculation results for different images

Images	Plaintext image			Ciphertext image		
	R	G	B	R	G	B
Cat	7.5297	7.7148	7.741	7.9992	7.9994	7.9993
Fruit	7.2515	7.7321	6.4726	7.9992	7.9992	7.9994

4 Conclusions

In this paper, a neuromorphic electromechanical system is constructed by combining the two-disk dynamo and the integrate-and-fire neuron model. The proposed five-dimensional autonomous system exhibits abundant and complex dynamical behaviors, including multiscroll hidden attractors, based on the analysis of multiple bifurcation parameters. These rich dynamics enable the system to effectively mimic the nonlinear characteristics of neuro-electrical activities coupled with mechanical motions, offering a new approach to explore the interaction between neural signals and mechanical movements. Furthermore, a novel chaotic image encryption scheme is designed based on the chaotic sequences generated by the proposed system. The corresponding results show that the encryption algorithm has high information entropy and strong key sensitivity,

guaranteeing reliable security in information protection. Overall, this work unifies neuromorphic modeling, electromechanical dynamics, and chaotic encryption into a coherent framework. The proposed system not only enriches the family of chaotic systems with hidden attractors but also provides a promising chaotic carrier for practical encryption applications. It exhibits good application prospects in artificial tactile devices, intelligent sensing, and secure communication and is expected to promote further interdisciplinary research in related fields.

Acknowledgments

This work is supported by the Ningxia Natural Science Foundation Project (No. 2024AAC01001), the National Natural Science Foundation of China (No. 12302070), the Natural Science Foundation of Ningxia Province (No. 2024AAC05002), and the Youth Science and Technology Talent Cultivation Project of Ningxia Province.

Author contributions

Fuqiang WU designed the research. Fuqiang WU and Huimin QI processed the corresponding data. Huimin QI wrote the first draft of the manuscript. Ying XU and Fuqiang WU helped to organize the manuscript. Fuqiang WU and Jun MA revised and edited the final version.

Conflict of interest

Fuqiang WU, Ying XU, Huimin QI, and Jun MA declare that they have no conflict of interest.

Declaration on the use of generative AI tools

The authors declare that no generative AI tools were used in the preparation of this manuscript.

Data availability

The data that support the findings of this study are available from the corresponding author upon reasonable request.

References

Lei Z, Guo Q, Wang CN, et al., 2025. Continuous energy exchange between magnetic fields supporting memristive neuron firing. *Journal of Zhejiang University-SCIENCE A (Applied Physics & Engineering)*, 26(8): 755-770. https://doi.org/10.1631/jzus.A2500150

Kamsma TM, Boon WQ, Ter Rele, et al., 2023. Iontronic neuromorphic signaling with conical microfluidic memristors. *Physical Review Letters*. 130: 268401. https://doi.org/10.1103/PhysRevLett.130.268401

Yang FF, Ma J, Wu FQ, 2024. Review on memristor application in neural circuit and network. *Chaos, Solitons & Fractals*, 187: 115361. https://doi.org/10.1016/j.chaos.2024.115361

Ma J, 2025. Biological neurons to neural circuit, review from physical perspective. *Nonlinear Dynamics*, 113(19): 25365-25387. https://doi.org/10.1007/s11071-025-11487-4

Shao Y, Wu FQ, Wang QY, 2025a. Excitability and synchronization of vanadium dioxide memristor-inspired neurons. *Mathematics and Computers in Simulation*, 233: 99–116. https://doi.org/10.1016/j.matcom.2025.01.022

Shao Y, Wu FQ, Wang QY, 2025b. Bursting dynamics and synchronization of neuromorphic systems with VO2 memristors and Josephson junctions. *Nonlinear Dynamics*, 113(24): 33907-33926. https://doi.org/10.1007/s11071-025-11757-1

Bonagiri A, Biswas D, Chakravarthy S, 2024. Coupled memristor oscillators for neuromorphic locomotion control: modeling and analysis. *IEEE Transactions on Neural Networks and Learning Systems*, 35(6): 8638-8652. https://doi.org/10.1109/TNNLS.2022.3231298

Dutta S, Parihar A, Khanna A, et al., 2019. Programmable coupled oscillators for synchronized locomotion. *Nature communications*, 10(1): 3299. https://doi.org/10.1038/s41467-019-11198-6

Wu FQ, Guo YT, Ma J, et al., 2023a. Synchronization of bursting memristive Josephson junctions via resistive and magnetic coupling. *Applied Mathematics and Computation*, 455: 128131. https://doi.org/10.1016/j.amc.2023.128131

Wu FQ, Meng H, Ma J, 2024. Reproduced neuron-like excitability and bursting synchronization of memristive Josephson junctions loaded inductor. *Neural Networks*, 169: 607–621. https://doi.org/10.1016/j.neunet.2023.11.012

Wu FQ, Yao Z, 2023b. Dynamics of neuron-like excitable Josephson junctions coupled by a metal oxide memristive synapse. *Nonlinear Dynamics*, 111(14): 13481-13497. https://doi.org/10.1007/s11071-023-08524-5

Wu FQ, Feng XS, 2025. Spatiotemporal dynamics in discrete memristive Josephson junction array with electric and magnetic couplings under a controllable energy injection. *Nonlinear Dynamics*, 113(20): 28207-28231. https://doi.org/10.1007/s11071-025-11528-y

An XL, Qiao S, 2021. The hidden, period-adding, mixed-mode oscillations and control in a HR neuron under electromagnetic induction. *Chaos, Solitons & Fractals*, 143: 110587. https://doi.org/10.1016/j.chaos.2020.110587

Yang FF, Xu Y, Ma J, 2023. A memristive neuron and its adaptability to external electric field. *Chaos: An Interdisciplinary Journal of Nonlinear Science*, 33: 023110. https://doi.org/10.1063/5.0136195

Wu FQ, Hu XK, Ma, J, 2022. Estimation of the effect of magnetic field on a memristive neuron. *Applied Mathematics and Computation*, 432: 127366.

https://doi.org/10.1016/j.amc.2022.127366

Xu Y, Jia Y, Ma J, et al., 2018. Collective responses in electrical activities of neurons under field coupling. *Scientific reports*, 8(1): 1349. https://doi.org/10.1038/s41598-018-19858-1

Xu Y, Ren GD, Ma J, 2023. Patterns stability in cardiac tissue under spatial electromagnetic radiation. *Chaos, Solitons & Fractals*, 171: 113522. https://doi.org/10.1016/j.chaos.2023.113522

Li YN, Ma J, Xie Y, 2024. A biophysical neuron model with double membranes. *Nonlinear Dynamics*, 112(9): 7459–7475. https://doi.org/10.1007/s11071-024-09452-8

Feng XS, Kang T, Wu FQ, 2025. Bursting dynamics in a bi-membrane neuron-like model with resistive switching and memristive coupling activated by energy flow. *Nonlinear Dynamics*, 113(11): 13727-13745. https://doi.org/10.1007/s11071-025-11111-5

Bao BC, Hu JT, Bao H, et al, 2023. Memristor-coupled dual-neuron mapping model: initials-induced coexisting firing patterns and synchronization activities. *Cognitive Neurodynamics*, 18(2): 539-555. https://doi.org/10.1007/s11571-023-10006-8

Yang FF, Ma J, Ren GD, 2024. A Josephson junction-coupled neuron with double capacitive membranes. *Journal of Theoretical Biology*, 578: 111686. https://doi.org/10.1016/j.jtbi.2023.111686

An XL, Xiong L, Shi QQ, et al., 2023. Dynamics explore of an improved HR neuron model under electromagnetic radiation and its applications. *Nonlinear Dynamics*, 111(10): 9509–9535. https://doi.org/10.1007/s11071-023-08320-1

An XL, Liu SY, Xiong L, et al., 2024. Mixed gray-color images encryption algorithm based on a memristor chaotic system and 2D compression sensing. *Expert Systems with Applications*, 243: 122899. https://doi.org/10.1016/j.eswa.2023.122899

Lai Q, Liu Y, 2025. A family of image encryption schemes based on hyperchaotic system and cellular automata neighborhood. *Science China Technological Sciences*, 68(3): 1320401. https://doi.org/10.1007/s11431-024-2678-7

Yang FF, An XL, Xiong L, 2022. A new discrete chaotic map application in image encryption algorithm. *Physica Scripta*, 97(3): 035202. https://doi.org/10.1088/1402-4896/ac4fd0

Kitio Kwuimy CA, Woafo P, 2007. Dynamics of a self-sustained electromechanical system with flexible arm and cubic coupling. *Communications in Nonlinear Science and Numerical Simulation*, 12(8): 1504-1517. https://doi.org/10.1016/j.cnsns.2006.03.003

Kitio Kwuimy CA, Woafo P, 2008. Dynamics, chaos and synchronization of self-sustained electromechanical systems with clamped-free flexible arm. *Nonlinear Dynamics*, 53(3): 201-213. https://doi.org/10.1007/s11071-007-9308-0

Drapaca CS, 2015. An electromechanical model of neuronal dynamics using Hamilton's principle. *Front. Cell. Neurosci.* 9: 271. https://doi.org/10.3389/fncel.2015.00271

Mbeunga NK, Nana B, Woafo P, 2021. Dynamics of array mechanical arms coupled each to a Fitzhugh-Nagumo neuron. *Chaos, Solitons & Fractals*. 153: 111484. https://doi.org/10.1016/j.chaos.2021.111484

Mboussi Nkomidio A, Noubissie S, Woafo P, 2014. Dynamics of arrays of legs powered by a discrete electrical model of nerve. *Physics Letters A*, 378: 857–862 https://doi.org/10.1016/j.physleta.2014.01.035

Kouami NM, Nana B, Woafo P, 2020. Analysis of array nanoelectromechanical beams driven by an electrical line of Josephson junctions. *Physica C: Superconductivity and its Applications*, 574: 1353658. https://doi.org/10.1016/j.physc.2020.1353658

Bullard E, 1955. The stability of a homopolar dynamo. *Mathematical Proceedings of the Cambridge Philosophical Society*, 51: 744–760. https://doi.org/10.1017/S0305004100030814

Rikitake T, 1958. Oscillations of a system of disk dynamos. *Mathematical Proceedings of the Cambridge Philosophical Society*, 54: 89–105. https://doi.org/10.1017/S0305004100033223

Cox A, 1968. Lengths of geomagnetic polarity intervals. *Journal of Geophysical Research*, 73(10): 3247-3260. https://doi.org/10.1029/JB073i010p03247

Cook AE, Roberts PH, 1970. The Rikitake two-disc dynamo system. *Mathematical Proceedings of the Cambridge Philosophical Society*, 68: 547–569. https://doi.org/10.1017/S0305004100046338

Ito K, 1980. Chaos in the Rikitake two-disc dynamo system. *Earth and Planetary Science Letters*, 51(2): 451-456. https://doi.org/10.1016/0012-821X(80)90224-1

Ershov SV, Malinetskii GG, Ruzmaikin AA, 1989. A generalized two-disk dynamo model. *Geophysical & Astrophysical Fluid Dynamics*, 47(1-4): 251-277. https://doi.org/10.1080/03091928908221824

Donato S, Meduri D, Lepreti F, 2009. Magnetic field reversals of the earth: A two-disk Rikitake dynamo model. *International Journal of Modern Physics B*, 23: 5492–5503. https://doi.org/10.1142/S0217979209063808

Guo YT, Song XL, Ma J, 2025a. Control electromechanical arms by using a neural circuit. *Nonlinear Dynamics*, 113(2): 1605–1622. https://doi.org/10.1007/s11071-024-10260-3

Guo YT, Ma J, 2025b. An electromechanical arm model controlled by artificial muscles. Science China Technological Sciences, 68(4): 1420403. https://doi.org/10.1007/s11431-024-2855-3

Guo YT, Wang CN, Ma J, 2024. Model approach of artificial muscle and leg movements. *Physics Letters A*, 529: 130069. https://doi.org/10.1016/j.physleta.2024.130069

Ma J, Guo YT, 2024. Model approach of electromechanical arm interacted with neural circuit, a minireview. *Chaos, Solitons & Fractals*, 183: 114925. https://doi.org/10.1016/j.chaos.2024.114925

Electronic supplementary materials

Section S1

中文概要

题　目： 神经元电路驱动机电系统的动力学及其应用

作　者： 吴富强[1,2]，徐莹[3]，祁慧敏[1]，马军[4]

机　构： [1]宁夏大学，数学与统计学院，中国银川，750021；[2]宁夏数学基础科学研究中心，中国银川，750021；[3]山东师范大学，数学与统计学院，中国济南，250014；[4]兰州理工大学，物理系，中国兰州，730050

目　的： 构建基于忆阻器的神经形态机电模型对仿生机电系统的发展具有重要意义，而现有研究关于双盘发电机与积分放电神经元相结合的研究较少。本文旨在构建一种基于双盘发电机和双积分放电神经元的仿生神经形态机电系统，探究其复杂动力学行为，并基于该系统设计混沌图像加密方案，为相关领域的实际应用提供新路径。

创新点： 1. 将双盘发电机与双积分放电神经元模型相结合，构建了一个自治神经形态机电系统，实现了神经电活动与机械运动的耦合模拟；2. 所构建的系统可通过调节可控参数呈现多卷隐藏吸引子，丰富了具有隐藏吸引子的混沌系统；3. 基于该神经形态机电系统生成的混沌序列，设计了一种新型混沌图像加密方案，提升了信息加密的安全性与可靠性。

方　法： 1. 通过分析系统的电流-电压关系，验证所构建的仿生机电系统中具有忆阻特性；2. 采用数值模拟方法，通过双参数分岔、李雅普诺夫指数和相图等分析手段，验证系统的复杂混沌行为；3. 基于系统生成的混沌序列设计图像加密方案，并通过相关测试验证该加密算法的性能与安全性。

结　论： 1. 构建的神经形态机电系统具有丰富复杂的动力学行为，可呈现多卷隐藏吸引子，能有效模拟神经电活动与机械运动耦合的非线性特性；2. 基于该系统设计的混沌图像加密方案具有高信息熵和强密钥敏感性，可保证信息保护的可靠安全性；3. 本研究不仅丰富了混沌系统类型，还为实际加密应用提供了有前景的混沌载体，在人工触觉装置、智能传感和安全通信领域具有良好应用前景，可推动相关领域的跨学科研究。

关键词： 非线性动力学；机电系统；忆阻器；加密